

<https://doi.org/10.1038/s42005-024-01622-9>

Near-critical dark opalescence in out-of-equilibrium SF₆



Valentina Martelli¹✉, Amaury Anquetil², Lin AI Atik², Julio Larrea Jiménez¹, Alaska Subedi³✉, Ricardo P. S. M. Lobo²✉ & Kamran Behnia²✉

The first-order phase transition between the liquid and gaseous phases ends at a critical point. Critical opalescence occurs at this singularity. Discovered in 1822, it is known to be driven by diverging fluctuations in the density. During the past two decades, boundaries between the gas-like and liquid-like regimes have been theoretically proposed and experimentally explored. Here, we show that fast cooling of near-critical sulfur hexafluoride (SF₆), in presence of Earth's gravity, favors dark opalescence, where visible photons are not merely scattered, but also absorbed. When the isochore fluid is quenched across the critical point, its optical transmittance drops by more than three orders of magnitude in the whole visible range, a feature which does not occur during slow cooling. We show that transmittance shows a dip at 2eV near the critical point, and the system can host excitons with binding energies ranging from 0.5 to 4 eV. The spinodal decomposition of the liquid-gas mixture, by inducing a periodical modulation of the fluid density, can provide a scenario to explain the emergence of this platform for coupling between light and matter. The possible formation of excitons and polaritons points to the irruption of quantum effects in a quintessentially classical context.

The thermodynamic boundary between the liquid^{1,2} and the gaseous states of matter ends at a critical point. Beyond this point, the substance becomes a supercritical fluid³, which is dense like a liquid and compressible like a gas⁴, and it is employed in numerous applications, such as extraction, purification, or separation of chemical species across different industries^{5,6}.

Critical phenomena⁷ has been studied for two centuries. As early as 1822, Charles Cagniard de la Tour observed the formation of a “nuage très épais” (a very thick cloud)⁸, during the liquefaction of the supercritical fluid. Four decades later, Thomas Andrews⁹, clearly identified the phenomenon: “...the surface of demarcation between the liquid and gas became fainter, lost its curvature, and at last disappeared. The space was then occupied by a homogeneous fluid, which exhibited, when the pressure was suddenly diminished or the temperature slightly lowered, a peculiar appearance of moving or flickering striae throughout its entire mass.”

Dubbed critical opalescence, this phenomenon was found to occur universally at the critical end point of a liquid-gas transition⁷. Einstein¹⁰ and, independently, Smolouchowski¹¹ identified its origin by noting that fluctuations in the density (and therefore fluctuations in the refractive index) drastically amplify at the critical point. A few years later, Ornstein and Zernike (OZ)¹² presented a more sophisticated treatment by introducing the pair-correlation function. A more elaborated version of the latter, taking

into account corrections induced by interactions, was proposed half a century later by Fisher¹³. This spectacular optical phenomenon^{14–16} is known to be one manifestation of the divergence of the correlation length at the critical point. The latter leads to singularities in a host of physical properties, including heat capacity, compressibility, viscosity and thermal conductivity¹⁷.

The idea that the supercritical fluid is not featureless has recently gained traction^{18–26} (See refs. 27,28 for alternative views). Several boundaries inside the supercritical fluid, crossovers and not thermodynamic transitions (the Widom line, the Fisher–Widom line, and the Frenkel line) have been proposed.

The dynamic response near the critical temperature is also affected by the competition between the critical slowing down of the heat transfer and the fast thermalization induced by the ‘piston effect’^{24,17}, an adiabatic thermalization via acoustic waves, first invoked to explain unexpected features in micro-gravity experiments²⁹.

With an easily accessible critical temperature ($T_c = 318.7$ K), and critical pressure ($P_c = 3.76$ MPa), sulfur hexafluoride (SF₆) is a popular platform for the study of the critical point^{30–32} (Fig. 1a, b). During a study of near-critical SF₆ subject, we found that when it is quenched below its critical temperature (following the trajectory sketched in Fig. 1c), photons in the

¹Laboratory for Quantum Matter under Extreme Conditions, Institute of Physics, University of São Paulo, São Paulo, Brazil. ²Laboratoire de Physique et d'Étude des Matériaux (ESPCI - CNRS - Sorbonne Université) PSL University, Paris, France. ³CPHT, CNRS, École polytechnique, Institut Polytechnique de Paris, Palaiseau, France. ✉e-mail: valentina.martelli@usp.br; alaska.subedi@polytechnique.edu; ricardo.lobo@espci.fr; kamran.behnia@espci.fr

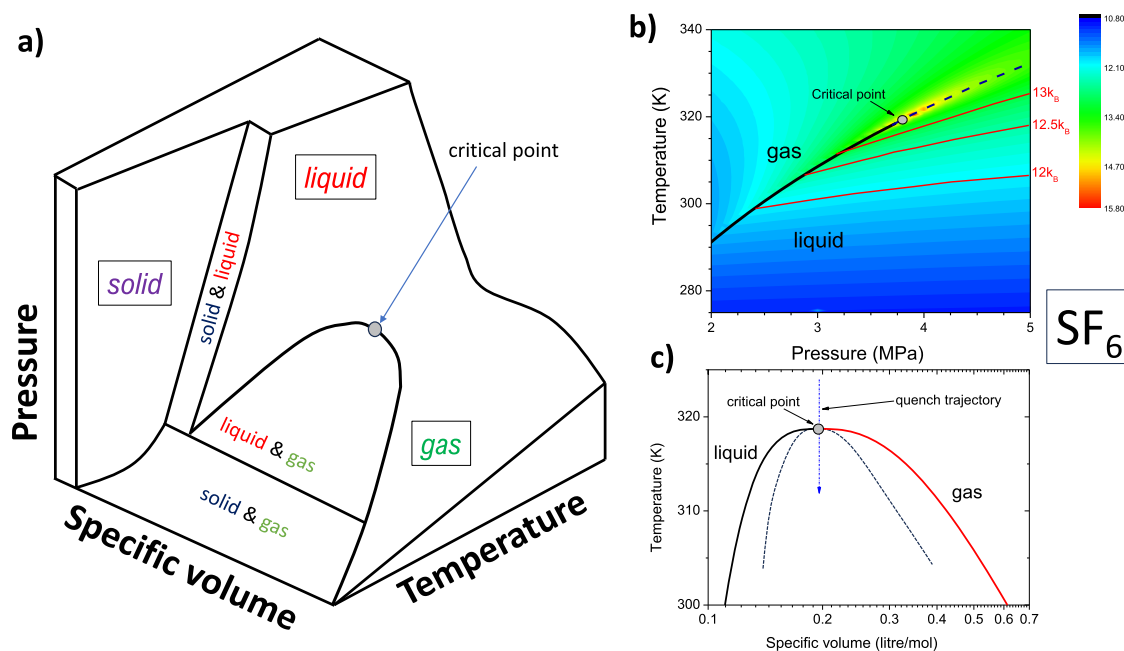


Fig. 1 | Phase diagram of SF_6 . **a** The generic pressure, temperature, volume (p, v, T) Gibbs surface showing the three phases, their coexistence and their boundaries. **b** Color plot of the isochore specific heat of SF_6 , c_V , in units of the Boltzmann constant near its critical point, according to the NIST database⁴². The melting curve (bold solid line) stops at the critical point and is followed by the Widom line (dashed line), identified by the peak in the specific heat data⁴³). Three lines corresponding to

specific c_V values are indicative of the crossover Frenkel line (See Introduction and Results sections). **c** The liquid-gas boundaries of SF_6 in the (temperature, specific volume) plane⁴². The dashed line is an approximate sketch of the spinodal line separating unstable and metastable regions of liquid-gas coexistence. Quenching the fluid at constant volume will push it to the spinodal region.

visible spectrum are absorbed and not merely scattered. The out-of-equilibrium fluid displays a black band of variable width, with details depending on the cooling rate and the relative orientation of pressure and temperature gradients. Measuring the transmittance across our 4-cm-thick fluid, we found that this blackness is concomitant with a large (four orders of magnitude) attenuation of the transmission coefficient and the appearance. For both slow cooling and fast cooling, we detect an absorption peak at 2 eV.

Critical opalescence, which refers to an amplified turbidity in a fluid kept at thermodynamic equilibrium and pushed to its critical point, is driven by the amplification of Rayleigh and Brillouin scattering of light. It has been experimentally quantified in the presence¹⁴ and in the absence³³ of gravity. Puglielli and Ford¹⁴ verified the OZ theory and quantified the correlation length of SF_6 from their data. In their micro-gravity experiment, Lecoutre et al.³³ quantified turbidity to within a fraction of millikelvin of the critical temperature and detected deviations from the OZ theory associated with particle-particle interaction, as proposed by Fisher¹³.

In contrast with these studies, we find that the out-of-equilibrium fluid during a quench becomes black and not merely turbid. One cannot explain this blackness, which is destroyed by reducing the cooling rate and approaching the thermodynamic equilibrium, within the framework of the OZ theory. We argue that the Coulomb attraction between electrons and holes is strong in our context providing a context for the formation of excitons^{34,35} and their interaction with photons in the visible spectrum. This constitutes a first step towards understanding the experimental observation, which still lacks a solid theoretical account.

A promising framework for our study is the Cahn-Hilliard theory of spinodal decomposition^{36–38}, which treats binary solids or liquid solutions quenched out of equilibrium. In our experiment, we force our fluid to a point in the phase diagram where the two (gaseous and liquid) phases have different specific volumes at thermodynamic equilibrium. The Cahn-Hilliard theory postulates that within the spinodal region (see the dashed lines in Fig. 1c), because of the absence of a thermodynamic barrier, the decomposition is governed by an ‘uphill’ diffusion. This leads to the emergence of spinodal nanostructures in metallic alloys³⁹ and in polymer blends⁴⁰. In our

case, the spatial modulation of the density generated by the quench may favor a type of light-matter coupling reminiscent of polaritons⁴¹ in solid state heterostructures.

Results

Observation of emergent darkness

Figure 1b presents a color map of the isochore specific heat (c_V) of SF_6 near its critical point in units of k_B , according to the NIST database⁴². The boiling line separating the liquid and the vapor phases ends at the critical point, where the Widom line starts. Here, it is plotted by tracking the experimentally resolved⁴² peak of the specific heat. The Frenkel line, separating the rigid and the non-rigid fluids^{19,43} is expected to be at lower temperature starting in the liquid state and eventually becoming parallel to the Widom line at higher temperature and pressure.

Our isochore investigation, along the trajectory sketched in Fig. 1c, used a pressure chamber filled with liquefied SF_6 gas commercially obtained from Leybold Didactic GMBH (Fig. 2a)⁴⁴.

We studied three different configurations where the temperature gradient across the chamber (∇T) and the pressure gradient (∇P) were either anti-parallel ($\nabla P \uparrow \nabla T$), perpendicular ($\nabla P \perp \nabla T$) or parallel ($\nabla P \downarrow \nabla T$), as depicted in panels b–d of Fig. 2. A Platinum sensor monitors the chamber’s temperature T_{pb} , and the gradient is obtained by flowing cooling water through the chamber (See section Methods for details).

A measurement protocol was defined and reproduced for each configuration: the chamber was heated up to 325 K and then cooled down at different rates. The fluid is in the supercritical state and is transparent [see right panels of Fig. 3a–c]. Upon cooling down phase separation occurs and the meniscus was observed by the camera.

Distinct behaviors were observed during warming up and cooling down [Fig. 3a–c]. Below T_c , the gas and liquid phases were visibly distinct. With warming, the meniscus slowly moves upward until it vanishes and leaves the full space for the supercritical phase.

Figure 3 shows a comparison of the evolution of transparency of SF_6 during a fast and a slow cooling process. In contrast with the quasi-static

Fig. 2 | The set-up and the three configurations.
a A picture of the chamber containing SF₆.
b–d Represent the three configurations explored in this work with different orientations of the temperature gradient with respect to the pressure gradient.

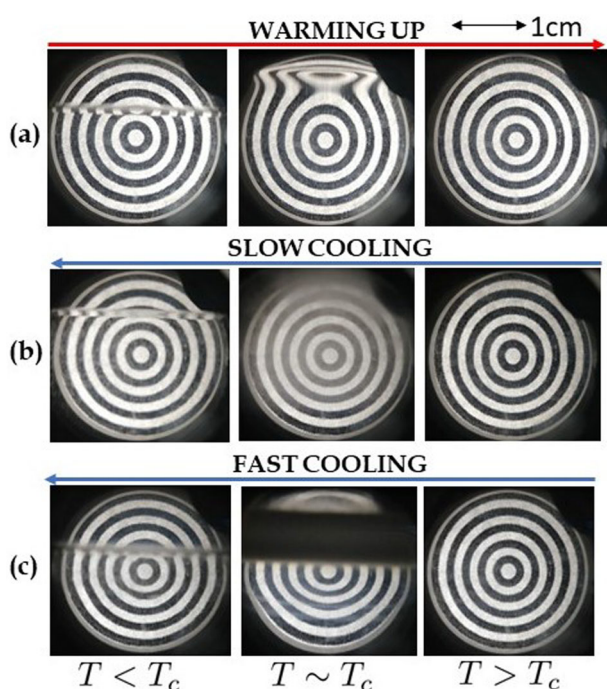
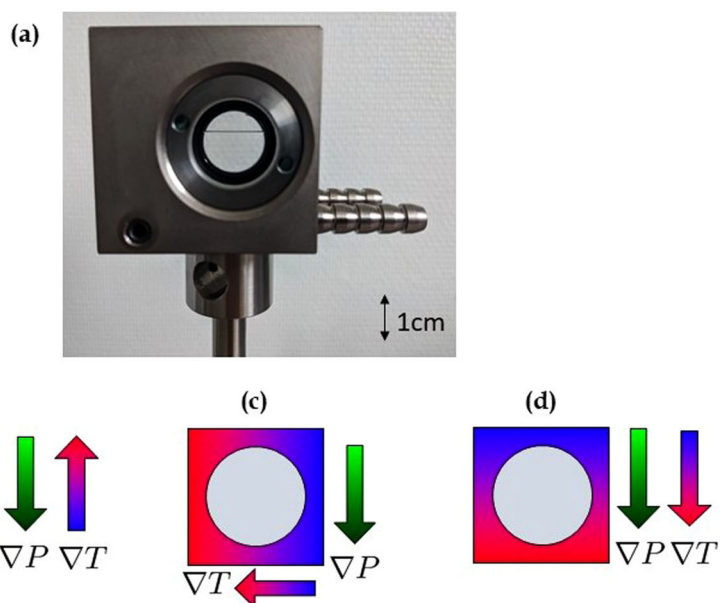


Fig. 3 | Warming, slow cooling and fast cooling. Concentric circles were put behind the back window of the chamber to show the evolution of transparency, with chamber in the $\nabla T \uparrow \nabla P$ configuration (See Supplementary Movies 1 and 2 (See Supplementary Materials for details)). **a** Evolution across the critical temperature during a warming process from $T < T_c$ to $T > T_c$. The phase separation fades away gradually, and the fluid remains transparent. **b** A slow cooling process in the reverse direction (from $T > T_c$ to $T < T_c$) reveals opacity near $T \sim T_c$. Despite turbidity, circles remain visible. **c** A dark band shows up during a fast cooling process (a quench across T_c). Fast and slow cooling frames sequences are reported for the other two configurations in Supplementary Movies 3, 4 ($\nabla P \perp \nabla T$) and Supplementary Movies 5, 6 ($\nabla P \downarrow \nabla T$) (See Supplementary Materials for details). Details on the Supplementary movies can be found in the Supplementary Note 3.

process, shown in Fig. 3b (See also Fig. 1 in ref. 17), in the fast-cooling process a black horizontal pattern abruptly appears [Fig. 3c] and then gradually fades away and is replaced by a meniscus separating the two distinct phases. The patterns depend on the cooling rate and configurations.

Visual recording of emergent darkness in the three configurations

The results obtained for the three configurations are presented in the next three Figs. 4–6. Frames were recorded during cooling down with a fixed sampling frequency together with the corresponding chamber’s temperature T_{Pi} ; an appropriate similarity index (mean squared error, MSE) is computed for each frame and compared with the initial frame (See Methods). We proceed to discuss each configuration.

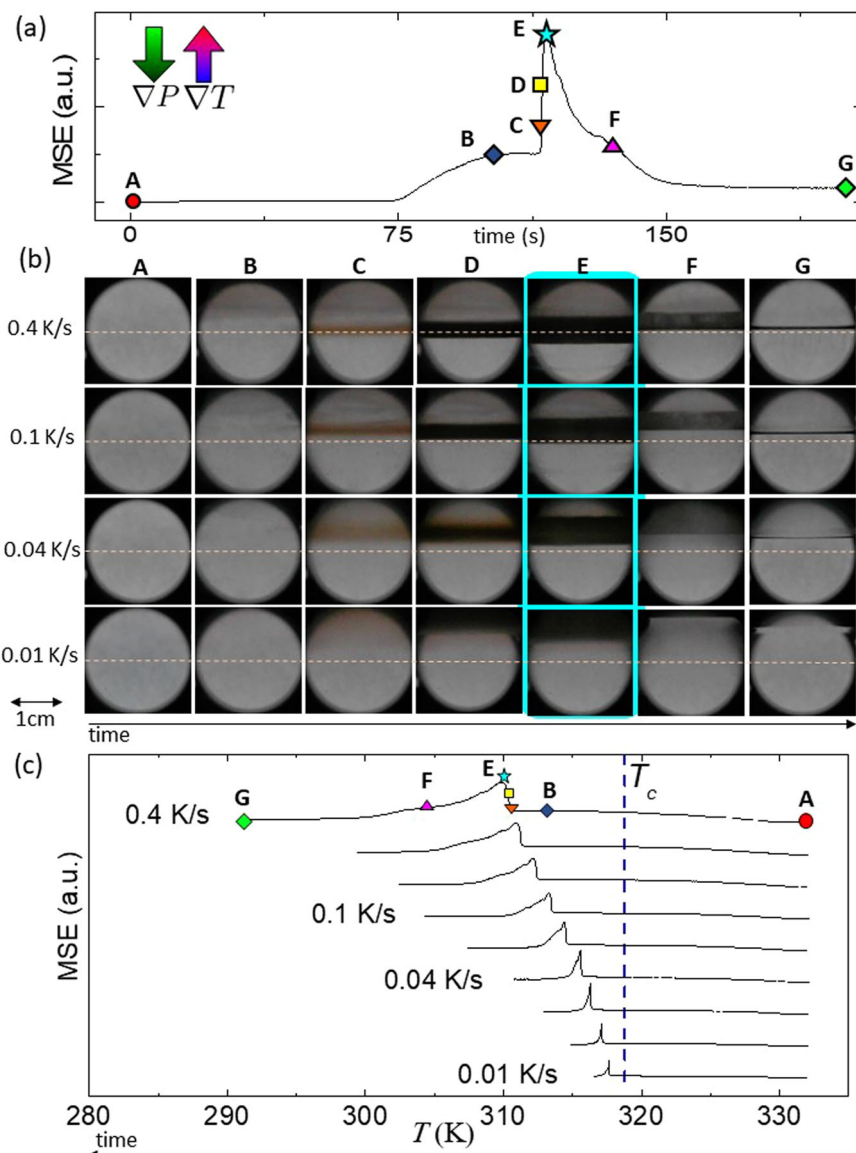
The anti-parallel configuration. Figure 4 shows the data for this configuration ($\nabla P \uparrow \nabla T$). Panel a shows the temporal evolution of the MSE-index (Eq. (6)) extracted from processing the image data together with the corresponding frames at selected instants of times (labeled from A to G) during a cooling rate of 0.4 K/s. The MSE index sharply peaks when the black pattern occupies the widest region. It is, therefore, a reliable quantifier of the black pattern evolution.

Figure 4b shows fluid picture frames during the cooling process. One can see that the temporal evolution of the blackness depends on the cooling rate. The evolution of the MSE index as a function of T_{Pi} is shown in Fig. 4c. For fast cooling, the sharp peak occurs well below the critical temperature. As the cooling rate slows down, the temperature at which the MSE index peaks and the blackness appears rises and becomes closer and closer to the critical temperature.

Frames A to G in Fig. 4b reveal a sequence of patterns. In frame B, there is a weak shadow on the upper side of the chamber; in C, a brownish horizontal pattern shows up and then becomes a dark black band in E. For fast cooling, the black horizontal band is centered in the chamber. As the cooling rate decreases, it shifts up toward the upper side of the chamber. At the lowest cooling rates (< 0.2 K/s), the black region shows up only from above.

The perpendicular configuration. Figure 5 shows the results for the $\nabla P \perp \nabla T$ configuration. The temporal evolution of the MSE index is shown in Fig. 5a. Its thermal evolution is displayed in Fig. 5c. They both differ from the previous configuration. In particular, the temperature at which the MSE index peaks is barely lower than the critical temperature and shows a much weaker dependence on the cooling rate. In picture frames of the fluid during the cooling [Fig. 5b], one can see qualitative differences with the previous configuration. A black region appears from above (frames B and C). For the fastest cooling rate, this black region gradually covers more than half of the surface. It then

Fig. 4 | $\nabla T \downarrow \uparrow \nabla P$ configuration. **a** Time evolution of the mean squared error index (MSE) as a function of time. Frames at selected points are labeled from A to G. **b** Comparison of the A to G frames for different cooling rates (0.4 K/s to 0.01 K/s). The blue background (behind the E frames) points to the maximum in MSE for each data set. **c** Temperature dependence of the similarity index (MSE). The red arrow points to the peak corresponding to the maximum extension of the black pattern. Data are shifted downward to allow visualization. The blue dotted line shows the position of the critical temperature T_c .



becomes gradually transparent and then the phase separation line emerges. In this configuration, when the cooling rate is lower than 0.02 K/s, the dark pattern is almost absent (see F). It is replaced by a blurred frame with no blackness.

The parallel configuration. The data for the last explored configuration ($\nabla T \downarrow \downarrow \nabla P$) is shown in Fig. 6. The time dependence of the MSE index [Fig. 6a], as well as its temperature dependence [Fig. 6c], show subtle differences compared to previous configurations. In particular, well after the peak and the separation between phases [between points F to G in Fig. 6a], there is a large noise indicating persistent turbulence. According to the cooling frames [Fig. 6b], the blackness is not spatially confined and occupies the whole frame. At the slowest cooling rates, there is no clear blackness at all and the MSE, instead of showing a sharp peak, displays a broad maximum near T_c [Fig. 6c]. It is followed by a turbulent process below the critical temperature.

Despite the identical cooling protocol, salient features of the collected data differ in the three cases; a detailed comparison of the evolution of the maximum of the MSE-index and the T_{Pr} as a function of cooling rate is reported in the Supplementary Note 2 (See Supplementary Materials for details).

Transmittance spectra

In order to quantify the full opacity effect, we measured the transmittance of the sample in the visible range in the perpendicular configuration for two extreme cooling rates (i.e. ~ 0.02 K/s and ~ 0.3 K/s). The data is shown in Fig. 7.

Figure 7a shows a selection (from spectra at 29 different temperatures) of measurements during a slow-cooling process, starting from the supercritical phase at 320 K. This process corresponds to images shown in the bottom row of Fig. 5b. The overall transmittance value decreases with temperature (orange curves), down to 318 K (green curve) then increases (blue curves) back to a value close to the initial measurement. The transmittance of the supercritical (320.8 K) and liquid (316.1 K) are very similar. There are two important features in this data. First, the overall transmittance decreases to about 35% of its maximum value. Even if, visually, this is barely noticeable and easily hidden by the turbid aspect of the mixed-phase, the transmittance does decrease by a large amount. A second, more interesting feature, is the appearance of a marked dip around 2 eV in the transmittance. The amplitude of this dip is small, suggesting either a very weak absorption from the whole sample or, alternatively, a sparse distribution of highly absorbing regions. This marked 2 eV absorption feature appears only in the mixed state. It is absent from both the supercritical and the liquid phases.

Fig. 5 | $\nabla T \perp \nabla P$ configuration. **a** Time evolution of the mean squared error index (MSE) as a function of time. Frames at selected points labeled from A to G. **b** Comparison of the A to G frames for different cooling rates (0.4 K/s to 0.01 K/s). The blue background (behind the D frames) points to the maximum in the MSE index for each data set. **c** Temperature dependence of the similarity index (MSE). The red arrow points to the peak corresponding to the maximum extension of the black pattern. Data are shifted downward to allow visualization. The blue dotted line shows the position of the critical temperature T_c .

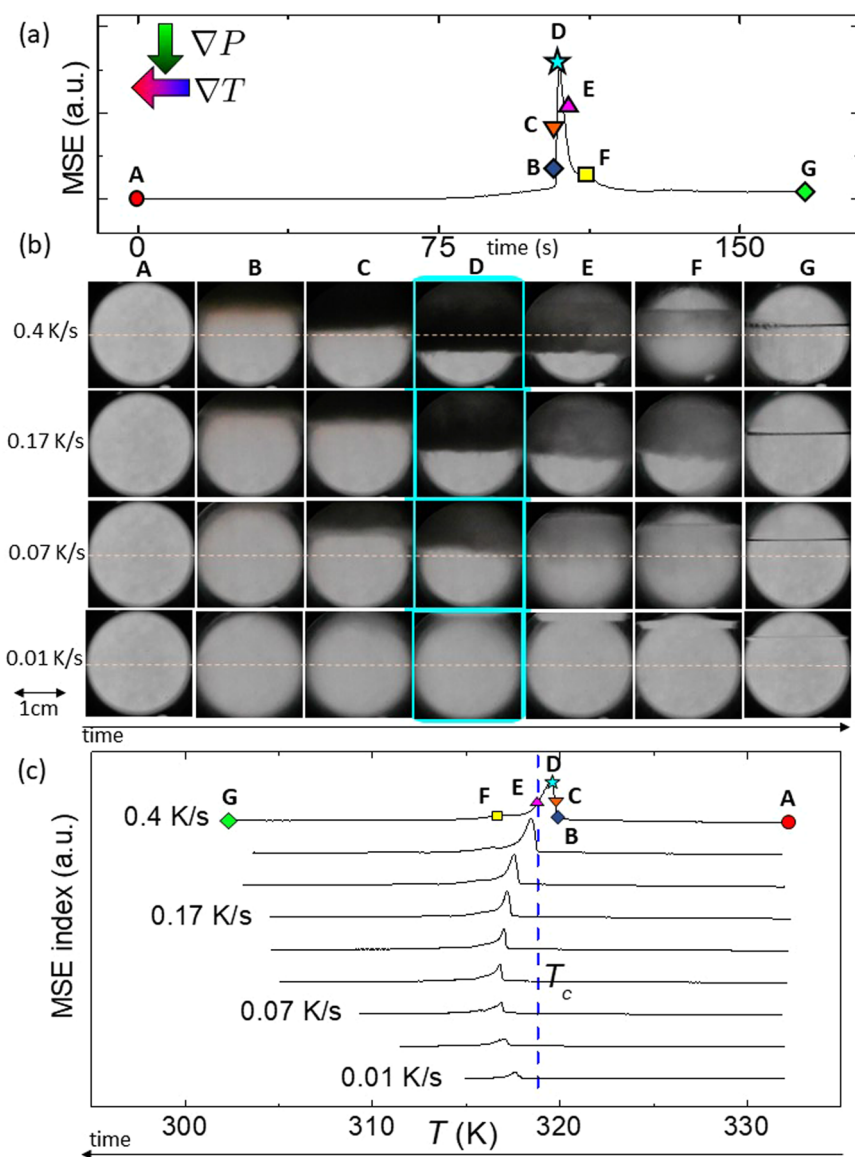


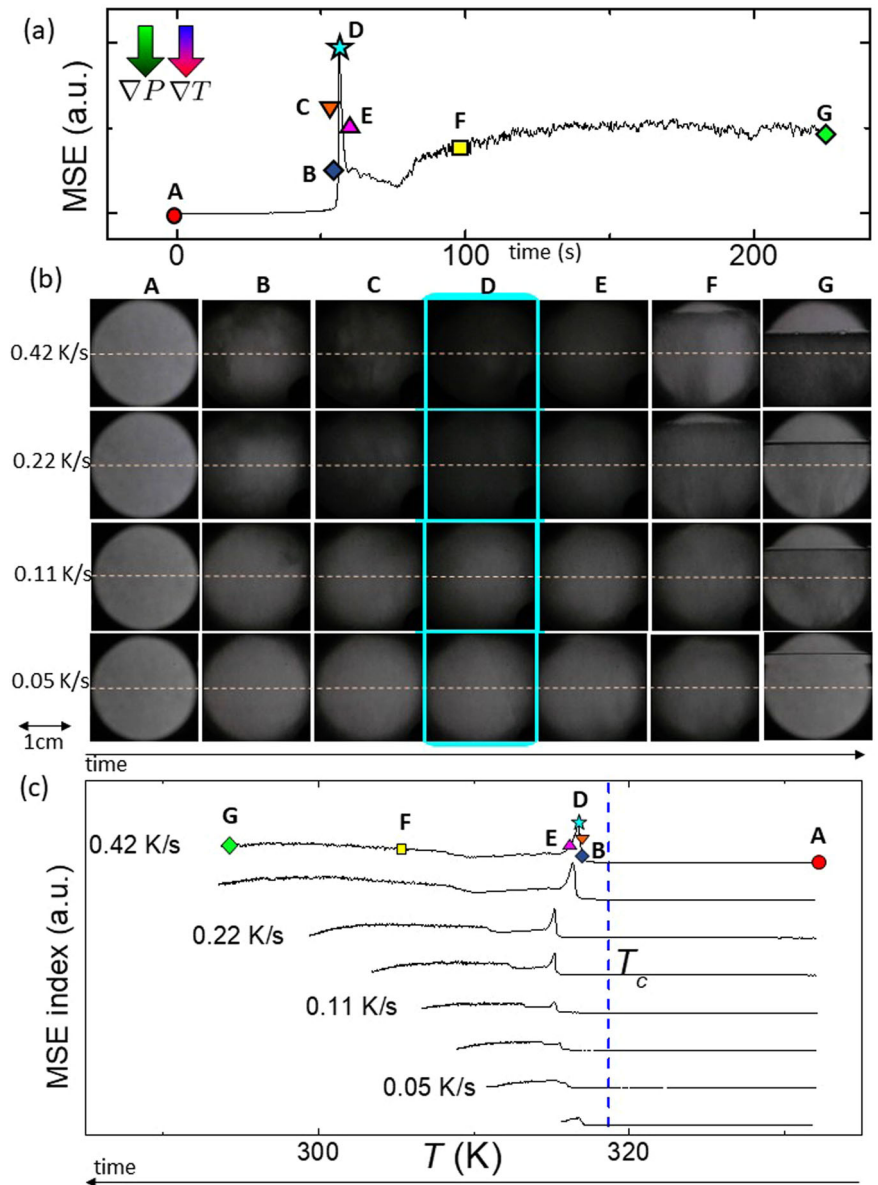
Figure 7b shows the transmittance when the sample is cooled at a fast rate of about 0.3 K/sec. Here the temperature is much less well defined as there is a large thermal gradient inside the chamber. We took 62 spectra over 90 s. The data is labeled with the delay after the cooling starting time. The initial overall behavior is the same. Starting from the supercritical phase, the transmittance decreases (red curves) and a dip in the vicinity of 2 eV appears. However, instead of having the transmittance saturating at about 35% of the initial value, here the sample goes fully opaque as shown by the green curved taken 28 s after cooling begins. The transmittance then increases again (blue curves) and the 2 eV dip remains well marked. The large thermal gradient in the chamber implies that we are far from an equilibrium state. As a consequence, this panel does not show the transmittance fully recovering to the liquid state transmittance. Nevertheless, if we wait a few minutes after cooling stops, the transmittance spectrum comes back to the regular spectrum of the liquid state. Figure 7c, we plot the fast cooling transmittance on a logarithmic scale. This figure shows that the system reaches full opacity faster than it recovers its transparency. In addition we see that, in the fast-cooling measurements, the transmittance is at least 4 orders of magnitude smaller than the one from the supercritical or the liquid phases. Note that the 10^{-5} – 10^{-4} range shown in this figure is a limitation of the CCD detector sensitivity rather than a measurement of the sample transmittance.

The absorption coefficient can be defined as $\alpha = -d^{-1} \log_{10} T$, where d is the sample thickness and T the transmittance (shown in panels a–c). Figure 7d shows the time dependence of α , taking $d = 4$ cm, at 3 selected energies – below (1 eV), above (3 eV), and at the minimum of the absorption peak (2 eV). The time dependence is essentially the same for the 3 energies. The fluid is in the supercritical phase at the delay time $t = 0$. We notice that the absorption coefficient increases slowly to about the 22 s mark where a steep rise gives a five-fold increase to α . It then still shows a sharp but slower decrease to the 40 s mark. From that point on, it takes a long time (a few minutes) for the transmittance to reach its liquid state equilibrium phase. This behavior is qualitatively the same as the one shown in Figs. 4–6 (note that the time scale is reversed in the data shown as a function of temperature). The shaded area in this panel shows the range of values that α takes in our quasi-static measurement, which is, at least, one order of magnitude smaller than the maximum α in fast-cooling spectra.

Previous observations of possibly related phenomena

We have found several reports in scientific literature reporting on darkness observed near a critical point. Garrabos et al. studied supercritical CO_2 under micro-gravity (10^{-4} times less than terrestrial gravity)⁴⁵ and observed a pattern of interconnected domains and rapid density fluctuations whose

Fig. 6 | $\nabla T \downarrow \downarrow \nabla P$ configuration. **a** Time evolution of the mean squared error index (MSE) as a function of time. Frames at selected points labeled from **A** to **G**. **b** Comparison of the **a** to **g** frames for different cooling rates (0.4 K/s to 0.04 K/s). The blue background (behind the **D** frames) points to the maximum in MSE for each dataset. **c** Temperature dependence of the similarity index (MSE). The red arrow points to the peak corresponding to the maximum extension of the black pattern. Data are shifted downward to allow visualization. The blue dotted line shows the position of the critical temperature T_c .



origin was not identified. In a related study, Guenoun and co-workers^{45,46} found black stripes in the images recorded slightly above T_c and attributed it to density gradients induced by a gravity of 2g. Simulations of a supercritical fluid under Earth gravity and with different orientation of thermal gradients were reported by Zappoli and collaborators^{47,48} (see Supplementary Discussion). Dark granular domains (each containing turbulent activity) were also observed. Ikier et al.⁴⁹ monitored cooling across T_c in SF₆, and observed droplets domains with dark circular regions constituting the meniscus between the liquid-gas separation at each droplet. The formation of such droplets under reduced gravity was studied in detail^{50,51}.

Discussion

Critical opalescence refers to the gradual enhancement of turbidity near the critical point when the latter is approached in thermodynamic equilibrium. Experiments both on Earth¹⁴ and in space³³ have documented this phenomenon. Our observation is qualitatively distinct. The blackness observed occurs when the two phases are separated and are amplified with an increasing cooling rate.

The Ornstein–Zernike theory of critical opalescence invokes Rayleigh and Brillouin scattering and the Lorenz-Lorentz relation⁵² linking the

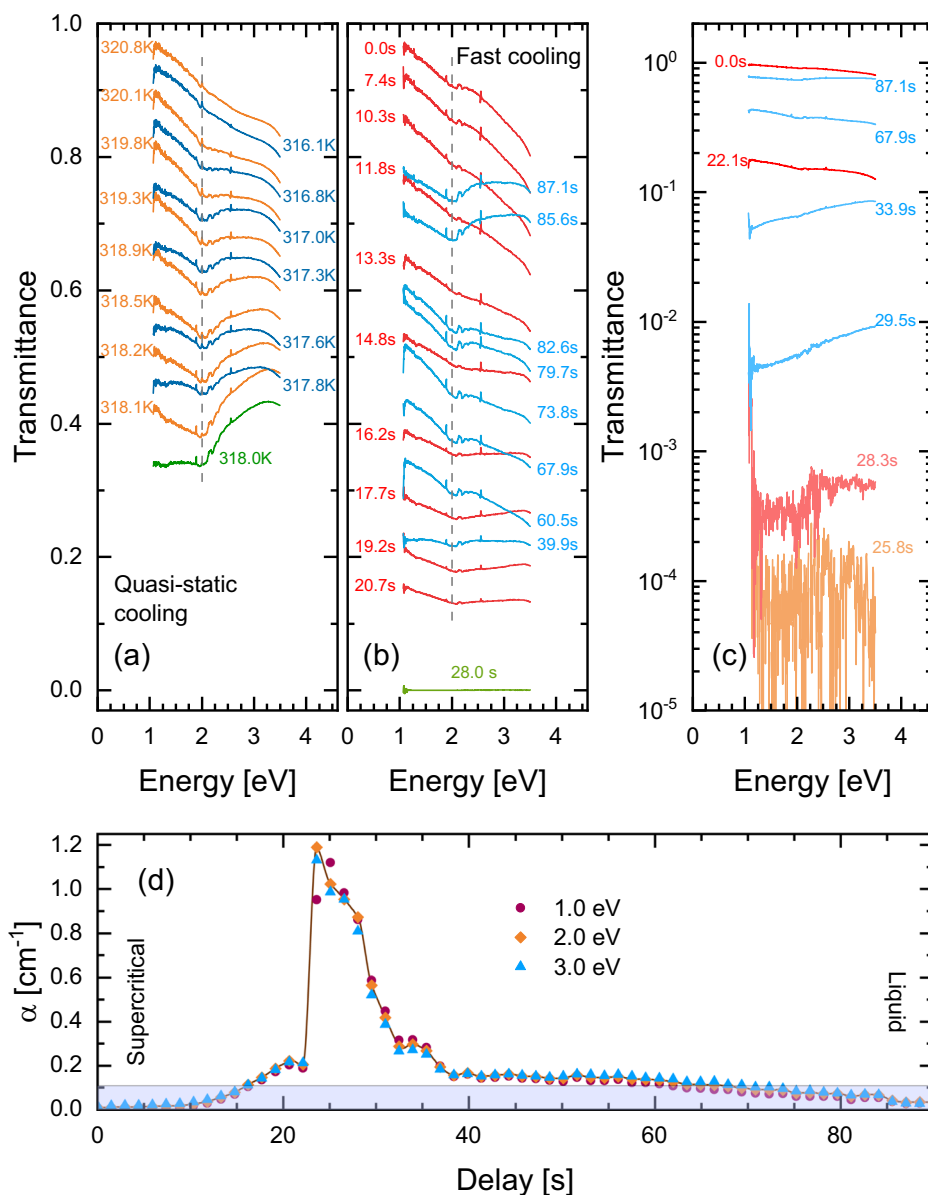
refraction index to density. Puglielli and Ford have shown that it leads to the following expression for the scattering rate¹⁴:

$$\tau_0 = \frac{8\pi^3}{3\lambda^4} \rho^2 \left(\frac{\partial \epsilon_r}{\partial \rho} \right)_T^2 k_B T_c \kappa_T. \quad (1)$$

Here, λ is the photon wavelength, ϵ_r is the electric permittivity of the medium, ρ is its density and κ_T is the isothermal compressibility. τ_0 has the dimensions of the inverse of length. Its temperature dependence is set by the temperature dependence of the compressibility which diverges at the critical point. The experimental validity of Eq. (1) near the critical point of SF₆ was experimentally confirmed on Earth, for $(T - T_c) > 0.03$ K¹⁴, and by very precise micro-gravity experiments to within $(T - T_c) \approx 0.3$ mK³³.

Our out-of-equilibrium data cannot be accounted for by this equation, which associates the amplification of τ_0 with the enhancement of the isothermal compressibility, (κ_T), and its divergence with the approach of the critical point. The wavelength of visible photons (400 nm < λ < 700 nm) and the critical temperature puts $\frac{8\pi^3}{3} \frac{k_B T_c}{\lambda^4}$ in the range of $10^7 - 10^8$ J·m⁻⁴. The order of magnitude of $\rho \frac{\partial \epsilon_r}{\partial \rho} \simeq \frac{\partial \epsilon_r}{\partial \ln \rho}$ is bounded by the Lorenz-Lorentz relation. In

Fig. 7 | Transmittance of the liquid or supercritical phases with respect to the gas phase. **a** Slow cooling from the supercritical (orange curves) to the liquid (blue curves) phase. The green curve shows the minimum value for the transmission. The top two curves, at 320.8 K and 316.1 K, show the transmission of the supercritical and the liquid phases, respectively. A small dip, absent from the end spectra, appears around 2 eV (shown by the vertical dashed line). **b** Fast (0.3 K/sec) cooling of the sample starting from 320 K over 90 s. The same 2 eV-dip from the quasi-static measurements appears in the mixed phase. However, contrary to the quasi-static measurement, the sample becomes fully opaque with a transmittance close to zero 28 s after cooling starts. **c** Fast-cooling transmittance in logarithmic scale. The lowest value for the transmittance is at least 4 orders of magnitude smaller (value limited by the detector sensitivity) than the transmittance of either the supercritical or the liquid phase. **d** Time-dependence of the absorption coefficient at selected photon-energies. The solid line is a guide to the eye. The delay time is measured from the supercritical phase at $t = 0$. The shaded area illustrates the range of values for α in the quasi-static measurements of panel (a).



this context, Eq. (1) would attribute the magnitude of $\tau_0 \approx 1 \text{ cm}^{-1}$ (seen during a fast cooling) to an unrealistically large compressibility (1 MPa^{-1}). It is unlikely that the bulk modulus of the fluid becomes suddenly as small as 1 MPa because of fast cooling. The bulk modulus supercritical SF_6 (at one degree off the critical temperature) is $\approx 60 \text{ MPa}^{53}$.

The spectral response brings an important piece to the puzzle. The liquid and supercritical phases are both essentially colorless transparent suggesting featureless transmittance in the visible range. Indeed, the transmittance at 320 K and 316 K of Fig. 7a do not show any absorption lines. The transparency of the end phases led to previous optical studies that looked at integrated or monochromatic transmittance measurements^{14,33}. The absence of absorption lines in the spectra impelled, naturally, a description of the critical opalescence in terms of light diffusion only.

However, in our measurements, near the critical point and only there, an optical absorption band, hence electrical-dipole-coupled transition, appears around 2 eV. The presence of an absorption peak shows that quantum mechanical processes (optical transitions) are at work.

In reasonably transparent media, the absorption coefficient is dominated by ϵ'' , the imaginary part of the dielectric function. A quantum-

mechanical dipole-transition formalism leads to⁵⁴:

$$\epsilon''(\omega) = \frac{4\pi n e^2}{m} \frac{\gamma \omega f_0}{(\omega_0^2 - \omega^2)^2 - \gamma^2 \omega^2}, \quad (2)$$

where ω_0 is the dipole-excitation resonance frequency, γ the resonance line-width (inverse lifetime). The parameter $f_0 = \frac{2m\omega_0}{\hbar} |\langle 0|x|n \rangle|^2$, dubbed the oscillator strength, is proportional to the induced dipole matrix element between the ground and excited states. It is fair to wonder what generates $\omega_0 \approx 2 \text{ eV}$ in our case.

The vibrational or rotational energy scales of single molecules are too low. The largest Raman-active mode of a SF_6 molecule is only $\approx 0.096 \text{ eV}^{55,56}$ and the strongest infrared absorption (which makes SF_6 a powerful green house gas) occurs near 0.117 eV^{57} .

On the other hand, the electronic band gap of the solid state is as large as 7 eV (See the band structural calculations in the Supplementary Note 1). This roughly quantifies the hopping energy of electrons across adjacent (van der Waals bound) SF_6 molecules and is expected to be relevant in a liquid phase of similar density. After all, optical gaps in crystalline and amorphous silicon have comparable amplitudes⁵⁸. We also note that the experimentally

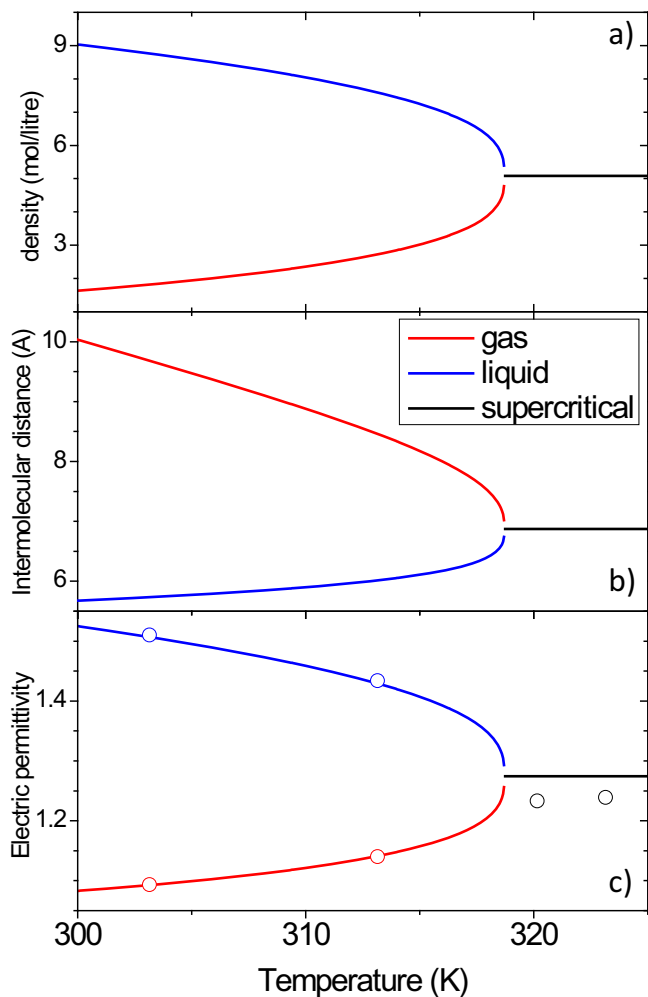


Fig. 8 | Density, intermolecular distance and electric permittivity. **a** The isochore density of SF₆ as a function of temperature near the critical point ref. 42. Below the critical temperature, the liquid and the gaseous phases have different densities. **b** The intermolecular distance calculated from the density for the three phases. **c** The electric permittivity, ϵ_r , of SF₆ as a function of temperature near the critical point for the three phases calculated from the density, using the Clausius–Mossotti expression and the polarization of the SF₆ molecule. Empty circles show the experimentally measured electrical permittivity of SF₆⁶².

resolved band gap in solid and liquid Xe are close to each other (≈ 9 eV)⁵⁹. More generally, the phonon theory of liquid thermodynamics⁶⁰ has recalled the existence of solid-like behavior in liquids in many aspects.

The ~ 7 eV hopping energy of electrons is much higher than the energy of visible photons (0.5–2 eV). This ab initio theoretical result is compatible with the absence of visible-energy optical transitions (absorption lines) in the transmittance and, more generally, with the transparency of the liquid and supercritical states.

In search for the source of the 2 eV energy scale, let us turn our attention to the dielectric constant of SF₆ (ϵ_r), which sets the amplitude of the screening of Coulomb potential. It is linked to the molecular polarizability, α , and the fluid density, N , through the Clausius–Mossotti relation:

$$\frac{\epsilon_r - 1}{\epsilon_r + 2} = \frac{N\alpha}{3\epsilon_0} \tag{3}$$

The density of the fluid near the critical point is available thanks to ref. 42 (see Fig. 8a). The extracted inter-molecular distances are shown in Fig. 8b. We have injected the density of fluid and the polarizability of SF₆ ($\alpha = 6.5 \text{ \AA}^{-3}$ ^{61,62}) in Eq. (3) to quantify ϵ_r of the three phases in our range of

interest. The result is shown in Fig. 8c. The experimentally measured values of ϵ_r ⁶² at several temperatures are also shown. The small ϵ_r paves the way towards the formation of excitons with a strong binding energy.

A hydrogenic pair of electrons and holes has an effective Bohr radius of:

$$a_B^* = \frac{4\pi\epsilon_r\epsilon_0\hbar^2}{e^2} \left(\frac{1}{|m_e|} + \frac{1}{|m_h|} \right) \tag{4}$$

With $\epsilon_r < 1.5$, $\frac{1}{m_e} \gg \frac{1}{m_h}$, and $m_e \approx m_0$, Eq. (4) yields an $a_B^* \approx 1 \text{ \AA}$, shorter than the distance between S and F atoms of the same molecule. Therefore, excitons are expected to be tightly bound. The energy of a Frenkel exciton^{63,64} is given by:

$$E_{exc}^F(d_{eh}) = \frac{e^2}{4\pi\epsilon_r\epsilon_0 d_{eh}} \tag{5}$$

Here, ϵ_0 is the vacuum permittivity, ϵ_r is the electric permittivity of the medium and d_{eh} is the distance between the electron and the hole.

We calculated the energy of Frenkel excitons according to Eq. (5) for the shortest possible d_{eh} . As shown in Fig. 9a, the separation between an F atom (locus of an electron) and an S atom (locus of a hole) is $a_1 = 1.57 \text{ \AA}$, which is when F and S atoms are on the same molecule. The next possibility is a_2 . It designates the distance between an S atom and an F atom located on adjacent molecules. In contrast to a_1 , a_2 varies with the fluid density. Figure 9b shows E_{exc}^F for these two types of excitons as a function of temperature, taking the extreme values of ϵ_r at each temperature.

The energy separation between a_1 and a_2 excitons is roughly 2 eV, close to the dip resolved by transmittance experiment. Thus, exciton formation near the critical point provides a possible explanation. We note that this is not the first case of exciton physics in a liquid. Tightly bound excitons have been detected in liquid Xe above its melting temperature⁵⁹.

The mechanism generating the darkness during a quench is yet to be identified. Fast cooling of the fluid kept at a constant volume below its critical temperature triggers spinodal decomposition^{36–38} of the fluid to its liquid and gaseous components with an intricate nanometric structure. This opens the window to other quantum phenomena.

Quantum confinement is well-known thanks to research on quantum dots. Clusters of hundreds to thousands of atoms enclosed in a foreign matrix can display optical properties distinct from the bulk material⁶⁵. Liquid droplets may also become optical micro-cavities capable of morphology-dependent resonances⁶⁶, a cradle for polaritons. The latter are hybrid quasi-particles arising from the interaction of light with electrical-dipole optical transitions^{67–69}. Following the detection of exciton-photon coupling in semiconductor microcavities three decades ago^{70–72}, multiple platforms for observing polaritonic phenomena have been reported. Basov et al.⁴¹ have recently listed at least 70 different types of polaritonic light-matter dressing effects.

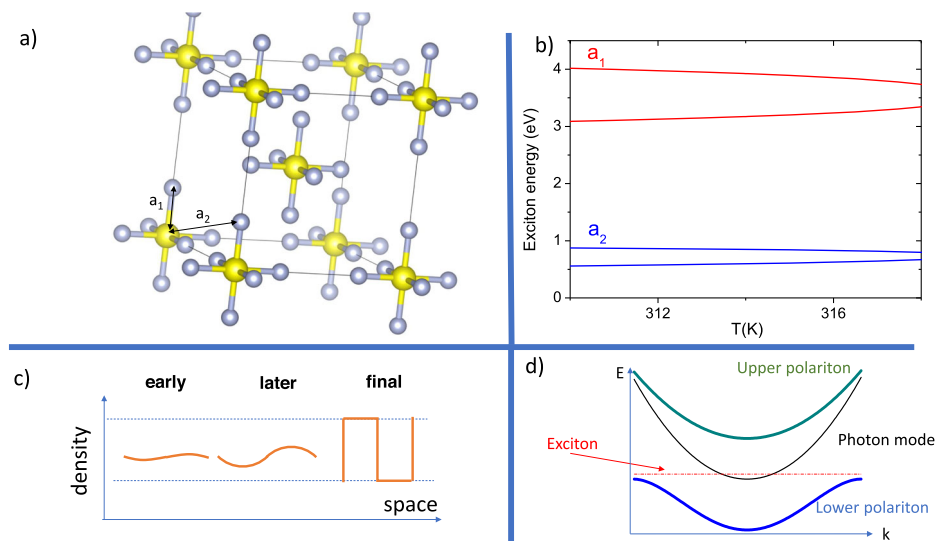
Spinodal decomposition is known to generate periodical modulation of the density of the relative composition of the two components of the fluid⁴⁰. This has been established in a variety of systems ranging from copper-nickel alloys³⁹ to polymers blends⁴⁰. The length scale of this modulation depends on physical properties and is generally measured in tens of nanometers. In contrast to nucleation and growth, the decomposition is a gentle, steady process with a steady increase in the local density gradient (see Fig. 9c), making it suitable for producing controlled structures at sub-micronic length scales⁷³.

It is tempting to speculate that when this process is triggered by quenching SF₆ to its spinodal phase, a liquid-gas morphology emerges which strengthens light-matter interaction. One possibility is that a gentle gradient of density leads to a multitude of barely separated exciton energy levels.

Conclusions

We found that when near-critical SF₆ is quenched, it becomes dark and its transmittance drops by, at least, four orders of magnitude. An optical transition appears in the vicinity of 2 eV. This case of pattern formation in

Fig. 9 | Excitons and their binding energies in SF₆. **a** SF₆ molecules in a body cubic centered configuration. Golden (silver) spheres represent S (F). *a*₁ and *a*₂ designate two radii for electron-hole pairs. The first length, *a*₁, is fixed, but *a*₂ increases with increasing intermolecular distance. **b** Upper and lower boundaries for exciton energies according to Eq. (5) for *d_{eh}* = *a*₁ and for *d_{eh}* = *a*₂ and given the variation of intermolecular distance with temperature. **c** A sketch of the evolution of density inhomogeneity during spinodal decomposition³⁹. The density gradient gently rises and eventually saturates to its full contrast. **d** The dispersion of an exciton, a cavity photon mode and the resultant hybrid states known as polaritons^{41,75,76}.



an out-of-equilibrium fluid is distinct from amplified turbidity caused by light scattering at thermal equilibrium in the vicinity of the critical point. The band gap of bulk SF₆ is too large, and the vibrational energy is too small to allow the absorption of visible light. Frenkel excitons with a separation level of ≈2 eV are expected to be there. It remains to be understood how the spinodal decomposition caused by the quench triggers darkness across a broad spectral range.

Methods

The SF₆ chamber

A Leybold Didactic GMBH pressure chamber (Fig. 2a) filled with liquefied SF₆ was used for the experiment⁴⁴. A platinum sensor placed into a lateral cavity allowed monitoring of the approximate temperature *T_{pt}* of the chamber. The latter is provided with two optical windows and inner pipes to circulate cooling water. The setup includes a light bulb in front of one of the two optical windows and a standard optical camera in front of the other one. The fluid images were recorded during the experiment. The circulation pipes were connected to a water bath with a controlled temperature. The arrangement allowed for setting a reproducible, stable, and uniform temperature of the chamber above *T_c* by heating.

The water circulation cools one side of the chamber before the other, generating a thermal gradient. Using an infrared camera, we verified (see the Supplementary methods (See Supplementary Materials for details)) the orientation of the temperature gradient as depicted in Fig. 2 for the three configurations. Since the cavity of the sensor is placed on the cold side of the chamber, in the following, the sensor temperature, *T_{pt}*, refers to the colder end of the temperature gradient. The chamber did not allow for modifications to host sensors inside itself. Therefore, the amplitude of the temperature gradient inside the fluid is known with limited accuracy.

The chamber was fixed on a small homemade optical table with dumping supports decoupling the fluid from external vibrations and could be oriented along three orientations. The pressure gradient (VP) due to gravity points downward and, using the critical mass density of SF₆ ($\rho_c = 742 \text{ kg}\cdot\text{m}^{-3}$) is estimated to be $\frac{dp}{dz} \simeq 7.3 \text{ Pa}\cdot\text{mm}^{-1}$.

Frames processing

The recorded images were processed through a Python routine comparing each frame by its precedent in order to quantify the observed variation as a function of time and *T_{pt}*. The frames were first translated in a scale of grays and then compared using the mean squared error (MSE) index, defined as

$$MSE = \frac{1}{mn} \sum_{j=0}^{n-1} \sum_{i=0}^{m-1} [I(i, j) - I_0(i, j)]^2 \quad (6)$$

where *I*(*i*, *j*) represents the intensity of the (*i*, *j*) pixel in a scale of grays quadratically summed over all the matrix columns and rows of the image with respect to the *I*₀(*i*, *j*) calculated at the initial conditions; (*m*, *n*) are the rows and columns that span the full matrix of pixels.

Optical spectroscopy transmission

Optical spectroscopy transmission measurements complemented the image recording experiments. We compared the transmittance across the fluid when it was cooled very slowly to when it was quenched rapidly below the critical point. Transmittance spectra in the visible range were collected from 1100 to 350 nm (1 to 3.5 eV) in an AvaSpec 2048-14 optical fiber dispersive spectrometer with a resolution of 2 nm. We utilized a deuterium-arc combined with a halogen lamp to cover this range. The spectrometer diffraction grating, combined with the sensitivity of the CCD detector, limits the low-energy range of the spectrum. The high-energy cut-off comes from the two glass windows of the chamber. The transmission of the liquid and the supercritical phases was normalized by the transmission of the gaseous phase measured at 315 K. All measurements were collected starting from the supercritical phase at 320 K. In the slow-cooling experiment, measurements were performed with 1000 averages of 2.17 ms-integration-time spectra. During the quench (i.e. fast cooling) experiment, the spectra-acquisition rate was decreased to 100 averages. All the spectra were collected in the (VP ⊥ VT) configuration.

Band structure calculations

The band structure calculations (See Supplementary Note 1 (See Supplementary Materials for details)) were performed using the generalized full-potential method as implemented in the WIEN2K package⁷⁴. Muffin-tin radii of 1.39 and 1.53 a.u. for S and F, respectively, were used. The plane-wave cutoff was set by $RK_{\text{max}} = 9$, where *K_{max}* is the plane-wave cutoff and *R* is the smallest muffin-tin radius used in the calculations. $16 \times 16 \times 16$ and $4 \times 4 \times 4$ *k*-point grid was used for the *Im3m* and *C2/m* phases, respectively, to perform the Brillouin zone integration in the self-consistent calculations.

Data availability

Data sets generated during the current study are available from the corresponding author on reasonable request. A selection of frame sequences is reported as Supplementary Movies.

Received: 16 December 2023; Accepted: 8 April 2024;
Published online: 25 April 2024

References

- Proctor, J. E. & Maynard-Casely, H.E. *The liquid and supercritical fluid states of matter* (CRC Press, Taylor and Francis, 2021).
- Trachenko, K. *Theory of Liquids* (Cambridge University Press, 2023).
- Callen, H. B. *Thermodynamics and an introduction to thermostatistics* (John Wiley & sons, 1998).
- Carès, P. A brief review of the thermophysical properties of supercritical fluids. *J. Supercritical Fluids* **53**, 2–11 (2010).
- Brunner, G. Applications of supercritical fluids. *Ann. Rev. Chem. Biomol. Engin.* **1**, 321–342 (2010).
- Knez, Željko Industrial applications of supercritical fluids: A review. *Energy* **77**, 235–243 (2014).
- Domb, C. *The Critical Point: A Historical Introduction To The Modern Theory Of Critical Phenomena* (CRC Press, 1996).
- de la Tour, C. C. Exposé de quelques résultats obtenus par l'action combinée de la chaleur et de la compression sur certains liquides, tels que l'eau, l'alcool, l'éther sulfurique et l'essence de pétrole rectifiée. *Ann. Chim. Phys.* **21**, 127–132 (1822).
- Andrews, T. On the continuity of the gaseous and liquid states of matter. *Philos. Trans. R. Soc. Lond.* **159**, 575–590 (1869).
- Einstein, A. Bemerkung zu der arbeit von d. mirimanoff: "Über die grundgleichungen ...". *Annal. Physik* **28**, 885 (1909).
- Smoluchowski, M. V. Molekular-kinetische theorie der opaleszenz von gasen im kritischen zustande, sowie einiger verwandter erscheinungen. *Annal. Physik* **330**, 205–226 (1908).
- Ornstein, L. S. & Zernike, F. Accidental deviations of density and opalescence at the critical point of a single substance. *K. Ned. Akad. Wetenschappen Proc. Ser. B Phys. Sci.* **17**, 793–806 (1914).
- Fisher, M. E. Correlation Functions and the Critical Region of Simple Fluids. *J. Math. Phys.* **5**, 944–962 (2004).
- Puglielli, V. G. & Ford, N. C. Turbidity measurements in SF₆ near its critical point. *Phys. Rev. Lett.* **25**, 143–147 (1970).
- Chu, B. Critical opalescence. *Ber. Bunsenges. Physikalische Chem.* **76**, 202–215 (1972).
- Zubkov, LeonidAleksseevich & Romanov, V. P. Critical opalescence. *Soviet Phys. Uspekhi* **31**, 328 (1988).
- Zappoli, B., Beysens, D. & Garrabos, Y. *Heat Transfers and Related Effects in Supercritical Fluids* (Springer, 2014).
- Brazhkin, V. V. & Trachenko, K. What separates a liquid from a gas? *Phys. Today* **65**, 68 (2012).
- Brazhkin, V. V., Fomin, Y. D., Lyapin, A. G., Ryzhov, V. N. & Trachenko, K. Two liquid states of matter: A dynamic line on a phase diagram. *Phys. Rev. E* **85**, 031203 (2012).
- Brazhkin, V. V. et al. "liquid-gas" transition in the supercritical region: Fundamental changes in the particle dynamics. *Phys. Rev. Lett.* **111**, 145901 (2013).
- Gorelli, F. A. et al. Dynamics and thermodynamics beyond the critical point. *Sci. Rep.* **3**, 1–5 (2013).
- Trachenko, K. & Brazhkin, V. V. Collective modes and thermodynamics of the liquid state. *Rep. Progr. Phys.* **79**, 016502 (2015).
- Ruppeiner, G., Dyjack, N., McAloon, A. & Stoops, J. Solid-like features in dense vapors near the fluid critical point. *J. Chem. Phys.* **146**, 224501 (2017).
- Ploetz, E. A. & Smith, P. E. Gas or liquid? the supercritical behavior of pure fluids. *J. Phys. Chem. B* **123**, 6554–6563 (2019).
- Trachenko, K., Baggioli, M., Behnia, K. & Brazhkin, V. V. Universal lower bounds on energy and momentum diffusion in liquids. *Phys. Rev. B* **103**, 014311 (2021).
- Cockrell, C., Brazhkin, V. V. & Trachenko, K. Transition in the supercritical state of matter: Review of experimental evidence. *Phys. Rep.* **941**, 1–27 (2021).
- Simeoni, G. G. et al. The Widom line as the crossover between liquid-like and gas-like behaviour in supercritical fluids. *Nat. Phys.* **6**, 503–507 (2010).
- Bryk, T. et al. Behavior of supercritical fluids across the "Frenkel Line". *J. Phys. Chem. Lett.* **8**, 4995–5001 (2017).
- Onuki, A., Hao, H. & Ferrell, R. A. Fast adiabatic equilibration in a single-component fluid near the liquid-vapor critical point. *Phys. Rev. A* **41**, 2256–2259 (1990).
- Wilkinson, R. A. et al. Equilibration near the liquid-vapor critical point in microgravity. *Phys. Rev. E* **57**, 436 (1998).
- Gorbunov, A., Emelyanov, V., Lednev, A. & Soboleva, E. Dynamic and thermal effects in supercritical fluids under various gravity conditions. *Microgravity Sci. Technol.* **30**, 53–62 (2018).
- Garrabos, Y. et al. Thermoconvective phenomena induced by vibrations in supercritical SF₆ under weightlessness. *Phys. Rev. E* **75**, 056317 (2007).
- Lecoutre, C., Garrabos, Y., Georgin, E., Palencia, F. & Beysens, D. Turbidity data of weightless SF₆ near its liquid-gas critical point. *Int. J. Thermophys.* **30**, 810–832 (2009).
- Frenkel, J. On the transformation of light into heat in solids. i. *Phys. Rev.* **37**, 17–44 (1931).
- Wannier, G. H. The structure of electronic excitation levels in insulating crystals. *Phys. Rev.* **52**, 191–197 (1937).
- Cahn, J. W. On spinodal decomposition. *Acta Metallurgica* **9**, 795–801 (1961).
- Cahn, J. W. Phase Separation by Spinodal Decomposition in Isotropic Systems. *J. Chem. Phys.* **42**, 93–99 (1965).
- Elliott, C. M. *The Cahn-Hilliard Model for the Kinetics of Phase Separation*, 35–73, (Birkhäuser, 1989).
- Findik, F. Improvements in spinodal alloys from past to present. *Mater. Des.* **42**, 131–146 (2012).
- Cabral, João T. & Higgins, J. S. Spinodal nanostructures in polymer blends: On the validity of the cahn-hilliard length scale prediction. *Progr. Poly. Sci.* **81**, 1–21 (2018).
- Basov, D. N., Asenjo-Garcia, A., Schuck, P. J., Zhu, X. & Rubio, A. Polariton panorama. *Nanophotonics* **10**, 549–577 (2021).
- National Institute of Standards and Technology database, <https://webbook.nist.gov/chemistry/fluid> (2023).
- Proctor, J. E., Pruteanu, C. G., Morrison, I., Crowe, I. F. & Loveday, J. S. Transition from gas-like to liquid-like behavior in supercritical n₂. *J. Phys. Chem. Lett.* **10**, 6584–6589 (2019).
- Pressure chamber for demonstrating the critical temperature. <http://www.leybold-shop.com> (2023).
- Garrabos, Y. et al. Observation of spinodal decomposition in a hypercompressible fluid under reduced gravity. *EPL Europhys. Lett.* **19**, 491 (1992).
- Guenoun, P. et al. Thermal cycle around the critical point of carbon dioxide under reduced gravity. *Phys. Rev. E* **47**, 1531 (1993).
- Zappoli, B., Amiroudine, S., Carles, P. & Ouazzani, J. Thermoacoustic and buoyancy-driven transport in a square side-heated cavity filled with a near-critical fluid. *J. Fluid Mech.* **316**, 53–72 (1996).
- Amiroudine, S. & Zappoli, B. Thermoconvective instabilities in supercritical fluids. *Compt. Rend. Mécanique* **332**, 345–351 (2004).
- Ikier, C., Klein, H. & Woermann, D. Optical observation of the gas/liquid phase transition in near-critical sf₆ under reduced gravity. *J. Colloid Interface Sci.* **178**, 368–370 (1996).
- Beysens, D. A. Kinetics and morphology of phase separation in fluids: The role of droplet coalescence. *Phys. A* **239**, 329–339 (1997).
- Oprisan, A. et al. Dimple coalescence and liquid droplets distributions during phase separation in a pure fluid under microgravity. *Eur. Phys. J. E* **37**, 1–10 (2014).
- Kragh, H. The Lorenz-Lorentz formula: Origin and early history. *Substantia* **2**, 7–18 (2018).
- Makarevich, L. A., Sokolova, O. N. & Rozen, A. M. Compressibility of SF₆ along the critical isochore (on the value of the critical exponent γ). *Soviet J. Exp. Theor. Phys.* **40**, 305 (1975).
- Tanner, D. B. *Optical Effects in Solids* (Cambridge University Press, 2019).

55. Rubin, B., McCubbin, T. K. & Polo, S. R. Vibrational raman spectrum of SF₆. *J. Mol. Spectrosc.* **69**, 254–259 (1978).
56. Aboumaja, A., Berger, H. & Saint-Loup, R. Analysis of the raman spectrum of SF₆. *J. Mol. Spectrosc.* **78**, 486–492 (1979).
57. Boudon, V. et al. Resolving the forbidden band of SF₆. *Phys. Chem. Chem. Phys.* **16**, 1415–1423 (2014).
58. Knief, S. & von Niessen, W. Disorder, defects, and optical absorption in a – Si and a – Si: H. *Phys. Rev. B* **59**, 12940–12946 (1999).
59. Steinberger, I. T. & Asaf, U. Band-structure parameters of solid and liquid xenon. *Phys. Rev. B* **8**, 914–918 (1973).
60. Bolmatov, D., Brazhkin, V. V. & Trachenko, K. The phonon theory of liquid thermodynamics. *Sci. Rep.* **2**, 421 (2012).
61. Hosticka, C. & Bose, T. K. Dielectric and pressure virial coefficients of imperfect gases: Hexadecapolar system. *J. Chem. Phys.* **60**, 1318–1322 (2003).
62. Kita, T., Uosaki, Y. & Moriyoshi, T. Static relative permittivity of sulfur hexafluoride up to 30 mpa. *Berichte Bunsenges. Physikalische Chem.* **98**, 112–118 (1994).
63. Knoester, J. & Agranovich, V.M. Frenkel and charge-transfer excitons in organic solids. In *Electronic Excitations in Organic Nanostructures*, vol. 31 of *Thin Films and Nanostructures*, 1–96 (Academic Press, 2003).
64. Zhu, X.-Y., Yang, Q. & Muntwiler, M. Charge-transfer excitons at organic semiconductor surfaces and interfaces. *Accounts Chem. Res.* **42**, 1779–1787 (2009).
65. Alivisatos, A. P. Semiconductor clusters, nanocrystals, and quantum dots. *Science* **271**, 933–937 (1996).
66. Giorgini, A., Avino, S., Malara, P., De Natale, P. & Gagliardi, G. Liquid droplet microresonators. *Sensors* **19**, 473 (2019).
67. Guillet, T. & Brimont, C. Polariton condensates at room temperature. *Comptes Rend. Phys.* **17**, 946–956 (2016).
68. Ribeiro, R. F., Martínez-Martínez, L. A., Du, M., Campos-Gonzalez-Angulo, J. & Yuen-Zhou, J. Polariton chemistry: controlling molecular dynamics with optical cavities. *Chem. Sci.* **9**, 6325–6339 (2018).
69. Forn-Díaz, P., Lamata, L., Rico, E., Kono, J. & Solano, E. Ultrastrong coupling regimes of light-matter interaction. *Rev. Mod. Phys.* **91**, 025005 (2019).
70. Weisbuch, C., Nishioka, M., Ishikawa, A. & Arakawa, Y. Observation of the coupled exciton-photon mode splitting in a semiconductor quantum microcavity. *Phys. Rev. Lett.* **69**, 3314–3317 (1992).
71. Houdré, R., Stanley, R. P., Oesterle, U., Illegems, M. & Weisbuch, C. Room-temperature cavity polaritons in a semiconductor microcavity. *Phys. Rev. B* **49**, 16761–16764 (1994).
72. Lidzey, D. G. et al. Strong exciton-photon coupling in an organic semiconductor microcavity. *Nature* **395**, 53–55 (1998).
73. Germack, D. S., Checco, A. & Ocko, B. M. Directed assembly of P3HT:PCBM blend films using a chemical template with sub-300 nm features. *ACS Nano* **7**, 1990–1999 (2013).
74. Blaha, P. et al. WIEN2k: An APW+lo program for calculating the properties of solids. *J. Chem. Phys.* **152**, 074101 (2020).
75. Carusotto, I. & Ciuti, C. Quantum fluids of light. *Rev. Mod. Phys.* **85**, 299–366 (2013).
76. Dovzhenko, D. S., Ryabchuk, S. V., Rakovich, Yu. P. & Nabiev, I. R. Light-matter interaction in the strong coupling regime: configurations, conditions, and applications. *Nanoscale* **10**, 3589–3605 (2018).

Acknowledgements

We thank Hervé Aubin, Daniel Baysens, Benoît Fauqué, Sandrine Ithurria Lhuillier, Arthur Marguerite, Xavier Marie, and Bernard Zappoli for stimulating discussions and critical remarks. V.M. acknowledges FAPESP(2018/19420-3). J.L.J. acknowledges FAPESP(2018/08845-3) and CNPq (310065/2021-6). K.B. is supported by the Agence Nationale de la Recherche (ANR-19-CE30-0014-04).

Author contributions

K.B. designed the research. A.A. and L.A.A. made the initial observation. Afterwards, V.M. and J.L.J. performed a detailed quantitative investigation of the emergent darkness in three different configurations. V.M. analyzed the frames of visual recordings and produced Figs. 3–6. RPSML measured and analyzed the transmittance spectra (Fig. 7). AS performed the band calculations. K.B. conceived Figs. 8 and 9. K.B., V.M., R.P.S.M.L. and A.S. wrote the paper, with feedback from all authors.

Competing interests

The authors declare no competing interests.

Additional information

Supplementary information The online version contains supplementary material available at <https://doi.org/10.1038/s42005-024-01622-9>.

Correspondence and requests for materials should be addressed to Valentina Martelli, Alaska Subedi, Ricardo P. S. M. Lobo or Kamran Behnia.

Peer review information *Communications Physics* thanks Cilian Cockrell and the other, anonymous, reviewers for their contribution to the peer review of this work. A peer review file is available.

Reprints and permissions information is available at <http://www.nature.com/reprints>

Publisher's note Springer Nature remains neutral with regard to jurisdictional claims in published maps and institutional affiliations.

Open Access This article is licensed under a Creative Commons Attribution 4.0 International License, which permits use, sharing, adaptation, distribution and reproduction in any medium or format, as long as you give appropriate credit to the original author(s) and the source, provide a link to the Creative Commons licence, and indicate if changes were made. The images or other third party material in this article are included in the article's Creative Commons licence, unless indicated otherwise in a credit line to the material. If material is not included in the article's Creative Commons licence and your intended use is not permitted by statutory regulation or exceeds the permitted use, you will need to obtain permission directly from the copyright holder. To view a copy of this licence, visit <http://creativecommons.org/licenses/by/4.0/>.

© The Author(s) 2024